Analyst

ROYAL SOCIETY OF CHEMISTRY

PAPER

View Article Online
View Journal

Cite this: DOI: 10.1039/d6an00096g

On-site amplification-free electrochemical detection of the plant pathogen *Xylella fastidiosa via* cathodic potential-induced DNA adsorption

Farjana Haque,[a] Kiran Shrestha,[a] Fatema Zerin Farhana,[a] Moutoshi Chakraborty,[b] Md Akeruzzaman Shaon,[a] Milkiyas Toru Tantu,[a] Omar Hamza Bin Manjur,[a] Sharmin Aktar,[a] Kevin M. Koo,[c] Tanveer Hussain,[d] Geoff M. Gurr[e] and Muhammad J. A. Shiddiky *[a]

Plant diseases pose a growing threat to global food security, with invasive bacterial pathogens presenting particular challenges for early detection and containment. *Xylella fastidiosa* is among the most destructive of these pathogens, infecting hundreds of plant species and posing a severe biosecurity risk to agricultural systems, including those in Australia. Despite its significance, routine detection still relies on laboratory-based molecular amplification methods that are slow, costly, and poorly suited to field deployment. Here, we present an amplification-free, proof-of-concept electrochemical method for detecting *X. fastidiosa* DNA based on potential-induced DNA adsorption onto a screen-printed gold electrode (Au-SPE). Target DNA is first isolated using magnetic beads and then rapidly adsorbed onto an Au-SPE through a 30 s cathodic potential step, enabling direct differential pulse voltammetric (DPV) readout without enzymatic amplification. The method clearly discriminates the *X. fastidiosa* 9a5c isolate from non-specific bacterial DNA (*Xanthomonas albilineans*), delivering a sensitive and selective signal within 2 minutes (30 s for adsorption plus 75 s for DPV measurement). The entire assay is completed in under 30 minutes, offering approximately fourfold faster analysis than conventional molecular amplification. When applied to spiked buffer and xylem sap (*i.e.*, a complex biological matrix) samples, the assay maintains high analytical performance, achieving a detection limit of 100 aM without compromising specificity or sensitivity. To support on-site testing, we also introduce a low-cost, 3D-printed device for rapid xylem sap extraction, allowing direct analysis with minimal handling and seamless integration into the detection workflow. Overall, the method provides a simple, rapid, and portable diagnostic strategy that advances plant pathogen detection beyond the laboratory. With further field validation, it could support earlier intervention and strengthen biosecurity surveillance for *X. fastidiosa* and other high-priority pathogens.

Received 27th January 2026,
Accepted 14th March 2026

DOI: 10.1039/d6an00096g

rsc.li/analyst

1 Introduction

Plant pest and pathogen associated diseases account for up to 40 percent of global food crop losses and cause more than US $220 billion in annual trade losses, posing a serious threat to food security, agricultural sustainability, ecosystem integrity, and societies in general.[1,2] Among these threats, the insect-transmitted and xylem-limited bacterium *Xylella fastidiosa* is regarded as one of the most destructive plant pathogens worldwide.[3,4] It infects more than 650 cultivated and wild plant species, including major food and fibre crops.[5–7] Originating in the Americas,[8] this highly invasive pathogen has now spread to parts of Europe and Asia, where it has caused serious environmental and economic damage.[9,10] In Australia, *X. fastidiosa* is recognised as the highest priority exotic plant pest under the national biosecurity framework, as there is no cure and many economically important crops are highly susceptible.[11,12] Early and rapid detection tools are therefore essential to support preparedness, surveillance, and timely response before irreversible damage occurs.

Detecting *X. fastidiosa* is particularly challenging because of its broad host range, long latent phase, insect vectors, and

[a]*Rural Health Research Institute (RHRI), Charles Sturt University, Orange, NSW 2800, Australia. E-mail: mshiddiky@csu.edu.au*
[b]*School of Environment and Science, Griffith University, Nathan, QLD 4111, Australia*
[c]*The University of Queensland Centre for Clinical Research (UQCCR), Brisbane, QLD 4029, Australia*
[d]*School of Science and Technology, University of New England, Armidale, NSW 2351, Australia*
[e]*Gulbali Institute & School of Agricultural, Environmental and Veterinary Sciences, Charles Sturt University, Orange, NSW 2800, Australia*

ability to spread silently while plants remain asymptomatic.[9,13–15] Several diagnostic methods are currently available, including molecular amplification-based polymerase chain reaction (PCR), loop mediated isothermal amplification (LAMP), enzyme linked immunosorbent assay (ELISA), and large scale airborne imaging approaches.[16–19] While these methods provide high sensitivity and specificity, they are largely laboratory based, require trained personnel, expensive reagents and instruments, and involve complex sample handling and logistics. These limitations restrict their use for rapid screening and on-site decision making, particularly in resource limited agricultural environments where early intervention is most critical.

The biology of *X. fastidiosa* further complicates detection because the bacterium resides exclusively within the xylem, where it adheres to the vessel wall, proliferates, and establishes structured biofilms that occlude water transport, thereby disrupting hydraulic conductivity and driving disease progression.[20] Effective early detection therefore requires access to biochemical information within deep vascular tissues rather than surface samples.[21] Although xylem sap represents a valuable matrix for pathogen detection and plant health surveillance, its collection remains technically challenging. Existing extraction approaches are frequently laborious, instrument-dependent, and prone to contamination, highlighting the need for simple, cost-effective, and field-deployable approaches for reliable sampling.[21–23] Consequently, the development of a simple 3D-printed device capable of rapidly extracting small volumes of xylem sap represents an important step toward practical and scalable early detection of plant and crop pathogens.

Conventional electrochemical DNA biosensors rely on probe-functionalized electrodes, which require time-consuming surface preparation and prolonged exposure to complex biological samples for target capture. During this exposure, non-target biomolecules compete for surface access, leading to non-specific adsorption that compromises assay specificity, sensitivity, reproducibility, and speed.[24] To overcome these challenges, DNA adsorption-based electrochemical biosensors have recently emerged as promising alternatives that use the intrinsic affinity between DNA and gold electrodes.[24–28] In these DNA adsorption-based assays, biological samples are kept physically separate from the sensing surface to enable independent isolation of the target DNA. The target DNA is initially isolated through magnetic capture and purification, and subsequently immobilised directly onto a bare Au-SPE. This strategy spatially separates complex biological matrices from the sensing interface, thereby minimising non-specific interactions and enhancing analytical performance. Notably, DNA adsorption-based assays operate without labels or enzymatic amplification, offering a simple and low-cost format that is well suited for field-deployable agricultural diagnostics.[29–32] However, a major limitation in DNA–gold affinity-based DNA sensors has been the slow DNA adsorption kinetics, typically requiring ~30 minutes. We recently showed that applying an external electric potential can dramatically accelerate DNA adsorption.[31] Using this method, the sample adsorption time was reduced to 1 minute for rapid detection of Ratoon Stunting Disease in sugarcane, establishing a practical pathway for extending DNA adsorption-based assay electrochemical sensing to *X. fastidiosa* while overcoming key constraints of speed, cost, and field deployability.

In this study, we introduce a potential-induced DNA adsorption-based electrochemical sensing method that maintains physical separation between plant samples and the electrode surface. The target DNA is magnetically captured and purified before a brief, potential-induced adsorption onto a bare Au-SPE. Electrochemical detection is performed using differential pulse voltammetry (DPV), which provides a sensitive and reliable measure of surface-adsorbed target DNA. In the presence of the ferricyanide quasi-reversible redox system ($[Fe(CN)_6]^{3-}$), changes in electron transfer at the Au-SPE reflect the extent of target DNA adsorption. Applying a cathodic potential of −500 mV *versus* Ag/AgCl for 30 s yields stable and reproducible signals, enabling semi-quantitative, amplification-free detection with high sensitivity. The simplicity and robustness of this cathodic potential-induced DNA adsorption method were demonstrated by integrating with a portable, low-cost xylem sap extraction device for on-field plant disease diagnostics. Beyond a single pathogen or crop, this strategy provides a general framework for rapid and early detection of plant diseases in resource-limited agricultural settings, with clear potential to reduce yield losses, strengthen biosecurity surveillance, and support sustainable farming practices.

2 Experimental

2.1 Materials and reagents

All chemicals and reagents were of analytical grade. Screen-printed gold electrodes (Au-SPE, DRP-250BT) with an integrated three-electrode system (Au working, Pt counter, and Ag reference electrodes) were obtained from Metrohm Dropsens (Llanera, Asturias, Spain). Nuclease-free water (Integrated DNA Technologies, Australia) was used for all aqueous solutions. Streptavidin-coated magnetic beads (Dynabeads MyOne Streptavidin C1), a HulaMixer™ sample mixer, a DynaMag™-2 Magnet, 5 M NaCl, 20× SSC buffer, 1 M Tris-HCl (pH 7.5), and 0.5 M EDTA (pH 8.0) were purchased from Invitrogen (Thermo Fisher Scientific). 2× SensiFAST SYBR No-ROX Master Mix was obtained from Meridian Bioscience (Cincinnati, OH, USA). Electrochemical measurements were performed using a DRP-DSC connector (Metrohm Dropsens) and a CH660E electrochemical analyzer/workstation (CH Instruments, Austin, TX, USA).

2.2 Synthetic target DNA and primer collection

Since *X. fastidiosa* is not present in Australia, synthetic DNA corresponding to the pathogen was used for proof-of-concept analytical validation. The synthetic target sequence spans bases 106 545 to 106 670 of the *X. fastidiosa* isolate 9a5c genome (NC_002488) within the *rimM* gene. A biotinylated

capture probe targeting a conserved 33 bp region of the *rimM* gene, forward and reverse primers,[17] and a non-specific target (NsT) synthetic DNA from *Xanthomonas albilineans* (bases 43 128 to 43 253 of the *XALB1* gene cluster, AJ586576.1) were obtained from Integrated DNA Technologies (IDT, Australia). Both of these species belong to the same family (*Xylella*) so they have a very high level of phylogenetic and ecological similarity.[33] The sequences of the synthetic target, capture probe, primers, and NsT are listed in Table S1. Specificity was confirmed by BLASTn screening against the NCBI nucleotide and genome databases,[34] with all sequences showing 100% homology to their intended targets. The target sequence we selected is conserved across all subspecies of *X. fastidiosa*, including *fastidiosa*, *multiplex*, *pauca*, *sandyi*, and *tashke*.

2.3 Xylem sap extraction device

Grapevine stems (*Vitis vinifera* L. 'Cabernet Sauvignon') were collected from vineyards in Orange, NSW 2800, Australia, on 4 June 2025 and transported to the laboratory in sterile containers. In the laboratory, leaves were removed, outer surfaces were wiped with 70% ethanol, and stems were cut into ~3 cm segments for sap extraction. The xylem sap collection device (Fig. 1A) was designed using Autodesk Inventor, sliced using Ultimaker Cura, and fabricated with an Ultimaker 3D printer. The assembled device consists of two rollers with textured grips, one connected to a rotating handle, and a PCR tube holder at the base. To operate the device, a PCR tube was first placed in the holder. A sterile plastic dropper (1–2 mL) was cut to the required size, and a cleaned stem segment was inserted. The dropper containing the stem was positioned between the rollers and pressed toward the PCR tube. Mechanical pressure was applied by rotating the handle counterclockwise, compressing the stem and collecting the xylem sap in the PCR tube. As the stem was squeezed, it gradually moved upward within the dropper while the sap accumulated in the tube (Fig. S1 and S2).

2.4 Probe hybridization and magnetic isolation

Stock lyophilized synthetic DNA sequences were resuspended according to the manufacturer's instructions (Integrated DNA Technologies, Inc.) to obtain a 100 μM stock solution, which was then diluted in nuclease-free water. Serial dilutions (1 nM to 100 aM) were prepared in nuclease-free water and in xylem sap to assess the performance of the developed method, with xylem sap samples simulating natural conditions. Each concentration was processed in triplicate, from target capture to detection. The *X. fastidiosa* capture probe-bead complex was prepared following the manufacturer's protocol. Streptavidin-coated magnetic beads were washed with 2× binding and washing (B&W) buffer (10 mM Tris HCL, pH 7.5; 1 mM EDTA, pH 8.0; 2 M NaCl) and incubated with the capture probe for 20 min at room temperature under gentle rotation using a HulaMixer™. Unbound probes were removed by washing with 1× B&W buffer. The target sequences were hybridized, isolated, and purified magnetically according to previously established protocols.[27,30,31] Briefly, the target DNA spiked into xylem sap

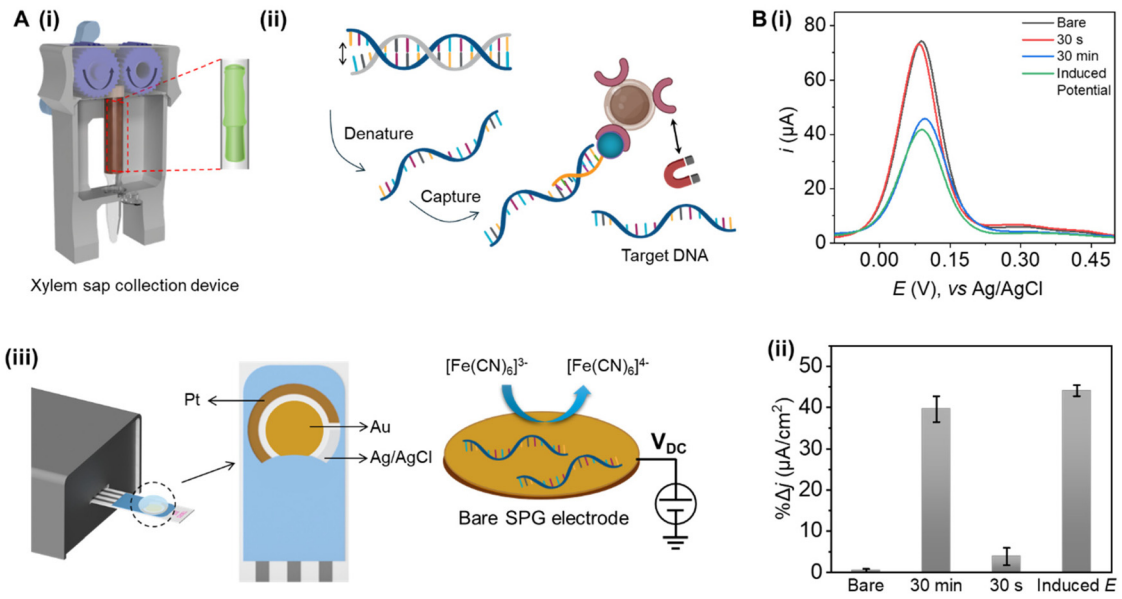

Fig. 1 Schematic illustration of the xylem sap extraction and magnetic capture–release workflow for electrochemical detection of *Xylella fastidiosa* stDNA. (A) (i) Computational design of the 3D-printed xylem sap extraction device. (ii) Target double-stranded DNA is denatured and selectively hybridised with biotinylated capture probes specific to *X. fastidiosa*, enabling magnetic isolation using streptavidin-coated beads. The captured DNA is thermally released and magnetically separated for downstream analysis. (iii) Electrochemical detection relies on potential-assisted adsorption of the target DNA onto an Au-SPE. (B) (i) DPV responses obtained under three conditions: 30 s incubation without applied potential, 30 min incubation without applied potential, and potential-assisted adsorption (–500 mV, 30 s) without incubation. (ii) Corresponding percentage decreases in current density. Error bars represent the SD from three independent DPV measurements performed using separately prepared electrodes.

was first denatured at 95 °C for 2 min using a calibrated heat block to generate single-stranded DNA (ssDNA), and immediately mixed with the capture probe-functionalized magnetic bead complex. The mixture was incubated at 55 °C to facilitate specific hybridization between the target and the capture probe. Following incubation, the bead–target complexes were washed with 2× B&W buffer to remove unbound species and resuspended in nuclease-free water. The target DNA was then thermally released from the beads, followed by magnetic separation to isolate the supernatant containing the released DNA. The isolated target DNA was diluted in 5× SSC buffer prior to adsorption and subsequent electrochemical measurements.[27] An identical procedure was applied to synthetic target DNA (stDNA) prepared in nuclease-free water, a non-specific target control, and a no-template control in which nuclease-free water was used in place of the target DNA.

2.5 Potential-induced DNA adsorption and electrochemical detection

All Au-SPE were electrochemically cleaned as previously described[35] and allowed to air-dry between measurements. The effective surface area of the working electrode was calculated using the Randles–Sevcik equation:[36]

$$i_p = 2.69 \times 10^5 n^{3/2} A D^{1/2} c v^{1/2} \quad (1)$$

where i_p is the peak current (A), n is the number of electrons transferred (n = 1), A is the effective area of the working electrode (cm^2), D is the diffusion coefficient of ferricyanide (7.60×10^{-5} cm^2 s^{-1}), c is the concentration (mol cm^{-3}), and v is the scan rate (V s^{-1}).

Magnetically isolated and purified target DNA (10 μL) was directly deposited onto the working electrode surface of the Au-SPE by applying a cathodic potential of −500 mV (*vs.* Ag/AgCl) for 30 s. After adsorption, the electrodes were rinsed three times with phosphate-buffered saline (10 mM PBS containing 137 mM sodium chloride and 2 mM potassium chloride, pH 7.4). For control experiments, DNA (10 μL) was passively deposited onto the working electrode surface of the A-SPE electrode without applying a potential.

DPV measurements of modified (target-adsorbed) and unmodified (bare) Au-SPE electrodes were performed in a 2 mM ferricyanide ($[Fe(CN)_6]^{3-}$) solution prepared in 10 mM PBS. DPV scans were recorded from −0.1 to 0.5 V using a pulse amplitude of 50 mV and a pulse width of 50 ms. The percentage decrease in current response was calculated as follows:

$$\%\,\Delta j = \left[\frac{j_{bare} - j_{adsorbed}}{j_{bare}}\right] \times 100\% \quad (2)$$

where j_{bare} and $j_{adsorbed}$ represent the current densities of the bare electrode and the electrode after DNA adsorption, respectively.

2.6 qPCR validation

Quantitative PCR (qPCR) was performed using a CFX96 Touch Real-Time PCR System (Bio-Rad Laboratories, Gladesville, NSW, Australia) to validate the electrochemical detection method. Magnetically isolated *X. fastidiosa* stDNA prepared in nuclease-free water and in xylem sap was used for comparison. A standard curve for quantification was generated by plotting cycle quantification (C_q) values against the logarithm of the stDNA concentration obtained from serial dilutions of *X. fastidiosa* stDNA. qPCR reactions were prepared according to the SensiFAST SYBR No-ROX kit protocol. Thermal cycling conditions consisted of polymerase activation at 95 °C for 3 min, followed by 40 cycles of denaturation at 95 °C for 5 s, annealing at 62 °C for 10 s, and extension at 72 °C for 20 s. C_q values were determined at the end of each run. Nuclease-free water was used as the no-template control, and *Xanthomonas albilineans* stDNA was used as a non-specific target control.

2.7 Statistical analysis

All data are presented as mean ± standard deviation (SD) from three independent experiments (n = 3). The limit of detection was calculated as the blank response plus three times the standard deviation of the blank. Data analysis and plotting were performed using OriginPro 2018 (OriginLab, Northampton, MA, USA) and Microsoft Excel 365. Figures were prepared using BioRender and Microsoft PowerPoint 365.

3 Results and discussion

3.1 Assay principle

Fig. 1A outlines the assay workflow for electrochemical detection of *X. fastidiosa* based on potential-induced DNA adsorption. Xylem sap is first collected using a 3D-printed extractor that gently expresses sap from the plant stem into a soft plastic tube, reducing the risk of external contamination [Fig. 1A(i)]. The sap is then used to prepare samples containing defined concentrations of *X. fastidiosa* stDNA. A biotin-labelled capture probe, complementary to the target sequence, is immobilised on streptavidin-coated magnetic beads. The bead-bound probe is incubated with *X. fastidiosa* stDNA to allow hybridisation. After hybridisation, magnetic separation and washing remove unbound DNA and nonspecific biomolecules, yielding purified probe–target complexes. The target stDNA is released from the capture probe by brief heating, following a published protocol [Fig. 1A(ii)]. The released stDNA is then directly adsorbed onto a bare Au-SPE by applying a short cathodic potential, which enables rapid surface attachment. Quantification of the adsorbed stDNA is performed by DPV using the ferricyanide quasi-reversible redox system [Fig. 1A(iii)].

Fig. 1B shows the DPV responses for the detection of 100 pM *X. fastidiosa* stDNA with and without application of an electric field. Without an electric field, a 30 s incubation produces less than a 5% decrease in current densities, indicating a small amount of DNA adsorption on the Au-SPE [Fig. 1B, red curve (i); third bar (ii)]. Extending this passive incubation to 30 min increases the current density decrease to ~40% [Fig. 1B, blue curve (i); second bar (ii)], consistent with greater

DNA adsorption driven solely by prolonged exposure. For both the cases, the attenuation of the faradaic current densities, which can be correlated semi-quantitatively with the surface coverage of adsorbed stDNA, arises primarily from two coupled mechanisms: (i) electrostatic (coulombic) repulsion between the negatively charged phosphate backbone of surface-bound stDNA and the anionic ferricyanide ions in solution, and (ii) steric blocking of electroactive sites, whereby adsorbed DNA physically limits the access of the $[Fe(CN)_6]^{3-/4-}$ species to the electrode surface. These effects impede interfacial electron transfer during the one-electron redox process, resulting in a reduced faradaic response relative to the bare electrode. Such current suppression mechanisms have been extensively reported for DNA-modified gold electrodes using ferricyanide ($[Fe(CN)_6]^{3-}$) as a redox probe.[24,37] In addition, DNA adsorption may induce local interfacial reorganisation, including changes in surface hydration, DNA conformation, or partial base–surface interactions, which can collectively influence heterogeneous electron-transfer kinetics.[38,39]

Application of a cathodic potential likely increases both the rate and extent of *X. fastidiosa* stDNA adsorption on the Au-SPE, resulting in a large decrease in DPV current density. As shown in Fig. 1B (green curve, (i); fourth bar (ii)), adsorption of 100 pM *X. fastidiosa* stDNA under an applied electric field produced an approximately 45% decrease in current density compared with measurements obtained in the absence of an electric field. Similarly, potential-induced adsorption of 1 pM *X. fastidiosa* stDNA resulted in an approximately 28% decrease in current densities relative to the blank, as shown in Fig. S3. These decreases arise from enhanced stDNA adsorption on the Au-SPE under potential, which may modify the electronic structure of the gold surface and the physicochemical properties of the electrode–electrolyte interface.[40]

Under cathodic bias, the surface electron density of gold may increase, shifting the surface Fermi level and potentially strengthening short-range non-covalent interactions with approaching DNA molecules.[41] The nucleobases of stDNA contain aromatic heterocycles with delocalised π-electron systems that may engage in weak charge-transfer, π–metal coupling, or dispersion interactions with the gold surface. Enhancement of surface electron density may increase the stabilization of these interactions, potentially raising the adsorption free energy[42] and promoting closer interfacial contact between the DNA bases and the electrode. This effect, combined with potential-induced restructuring of the electrical double layer, may facilitate accumulation of solvated cations near the negatively polarised surface.[43,44] These cations can partially screen electrostatic repulsion between the DNA phosphate backbone and the electrode, supporting DNA approach and transient interfacial confinement.

In addition, the local electric field may induce interfacial polarisation of the stDNA and promote charge redistribution at the DNA–gold contact region. This likely reinforces van der Waals and electrostatic stabilisation without the formation of covalent bonds.[45,46] Importantly, these interactions are likely reversible and consistent with field-assisted physisorption rather than chemisorption or thiol-mediated attachment, as previously observed for DNA adsorption at gold surfaces under mild conditions.[47,48] The combined effects of enhanced surface electronic coupling, double-layer screening, and field-induced polarisation substantially reduce the energetic barrier to adsorption and accelerate adsorption kinetics. As a result, brief cathodic potential steps enable rapid and efficient stDNA adsorption on bare Au-SPEs, in contrast to passive adsorption processes that rely on slow diffusion and weak interfacial interactions.

3.2 Optimization of parameters for potential-induced adsorption

The DPV response depends directly on the amount of stDNA adsorbed onto the Au-SPE. For a potential-induced DNA adsorption-based DPV readout to produce meaningful signal modulation, the surface coverage of adsorbed stDNA must remain within a moderate range. Excessive DNA loading leads to extensive surface passivation, which restricts access of the redox probe to the electrode interface and results in higher signal difference relative to the bare electrode. Accordingly, this assay operates optimally at low to moderate target concentrations that yield partial surface coverage, allowing reproducible current attenuation while preserving sufficient electroactive area for the ferricyanide quasi-reversible redox system to generate a measurable faradaic response. Optimization of the adsorption parameters therefore plays a critical role in achieving a rapid, reproducible, and sensitive assay.

To determine the optimal cathodic potential for stDNA adsorption, potentials ranging from 0 to −700 mV (*vs.* Ag/AgCl) were tested while maintaining a constant adsorption time of 30 s (Fig. 2A and A′). As the cathodic potential was increased from −100 to −500 mV, stDNA adsorption on the Au-SPE increased gradually, resulting in a corresponding increase in DPV current density decrease. At potentials more negative than −500 mV, the decrease in current density reached a plateau, consistent with near-maximum surface coverage by 100 pM *X. fastidiosa* stDNA. At potentials beyond −700 mV, minor gas evolution was observed, resulting in unstable and noisy DPV signals. Therefore, −500 mV was selected as the optimal potential, as it maximized DNA adsorption while avoiding hydrogen evolution and maintaining stable, reproducible DPV responses.

The effect of adsorption time was also investigated at a fixed cathodic potential of −500 mV (*vs.* Ag/AgCl) by varying the duration from 5 to 60 s (Fig. 2B and B′). Increasing the adsorption time from 5 to 30 s led to a gradual increase in stDNA adsorption and a corresponding increase in current density decrease. Beyond 30 s, no further change in current density was observed, indicating saturation of stDNA adsorption under these conditions.

Based on these results, the optimal conditions for potential-induced adsorption of *X. fastidiosa* stDNA were selected as −500 mV (*vs.* Ag/AgCl) applied for 30 s. Under these conditions, the assay produced a larger current density attenu-

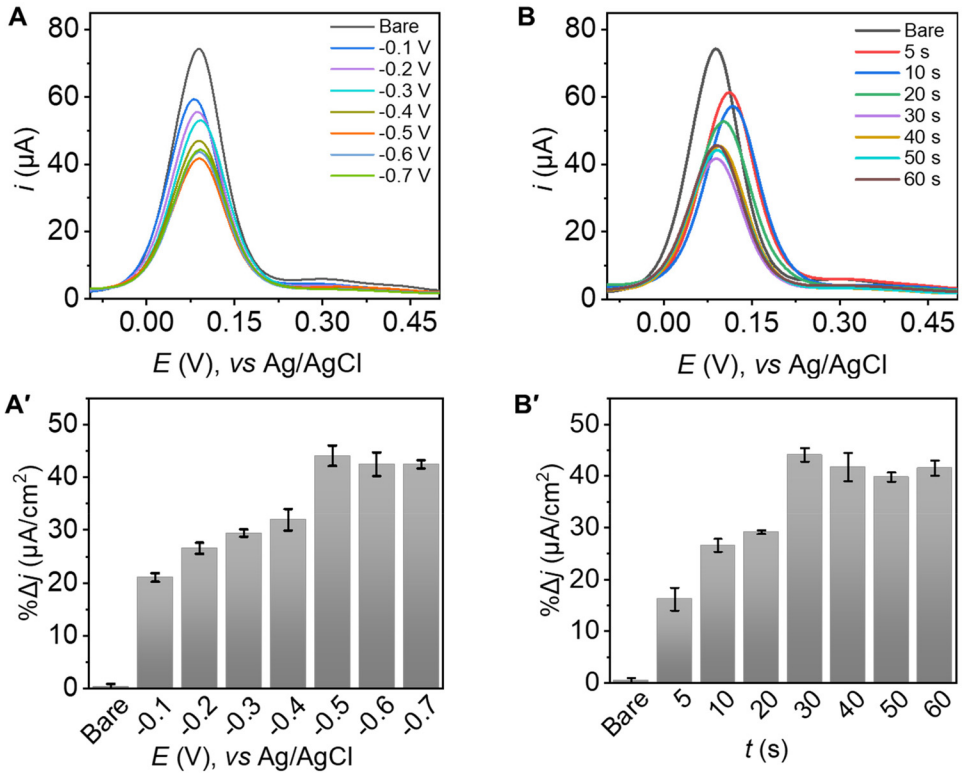

Fig. 2 Optimization of applied potential (A and A′) and adsorption time (B and B′) for potential-assisted adsorption of magnetically isolated 100 pM *Xylella fastidiosa* stDNA onto an Au-SPE. (A) Representative DPV responses obtained under cathodic potentials of −100 to −700 mV (*vs.* Ag/AgCl) applied for 30 s. (A′) Corresponding percentage decreases in current density. (B) Representative DPV responses recorded at −500 mV (*vs.* Ag/AgCl) for adsorption times ranging from 5 to 60 s. (B′) Corresponding percentage decreases in current density. Error bars represent the SD from three independent DPV measurements performed using separately prepared electrodes.

ation than that of the passive adsorption of *X. fastidiosa* stDNA on gold electrodes without potential for over 30 min, demonstrating the superior speed (30 s *versus* 30 min; Fig. 1B) and efficiency (approximately 45% *versus* 40%; Fig. 1B) of the potential-induced adsorption strategy.

In this study, the electrolyte composition was kept constant to allow the influence of the applied potential on nucleic acid adsorption and the resulting electrochemical response to be examined in isolation. The chosen potential window was selected to maintain stable ferri/ferrocyanide redox behaviour while avoiding the onset of gas evolution at more negative biases, thereby ensuring reliable signal interpretation. At the same time, nucleic acid adsorption at gold interfaces is expected to depend on electrolyte properties, including ionic strength and cation identity, which can modulate electrostatic screening and interfacial organization. Although these parameters were not studied here, their influence warrants systematic examination. Future studies exploring monovalent and divalent cations, controlled adjustment of ionic strength, and refined tuning of the potential window may provide further insight into the interfacial mechanism and help define the operational limits of the platform. Such investigations would contribute to facilitate consistent performance across diverse sample matrices and deployment settings.

3.3 Assay specificity

To evaluate assay functionality and specificity, we performed a series of control experiments (Fig. 3A). These included a no-template control (NoT), where buffer replaced the *X. fastidiosa* target; a no-beads control, where magnetic beads were omitted while capture probes were retained; and a no-capture-probe control (No CP), where capture probes were excluded from the isolation step.

All controls produced only negligible changes in current density, confirming the proper functioning of the assay. Assay specificity was first examined using a non-specific stDNA (NsT) sequence from *X. albilineans*, a closely related species within the same family (*Xanthomonadaceae*)[33] as *X. fastidiosa*. Both bacteria are xylem-limited, Gram-negative organisms that have undergone convergent reductive evolution. At both 1 nM (NsT high) and 100 aM (NsT low), *X. albilineans* NsT produced only marginal current changes, comparable to the NoT response, demonstrating high assay specificity (Fig. 3A).

Specificity was further tested using mixtures of *X. fastidiosa* stDNA and *X. albilineans* NsT across a range of concentrations:100 aM *X. fastidiosa* + 100 aM NsT (Xf low + NsT low), 100 aM *X. fastidiosa* + 1 nM NsT (Xf low + NsT high), 1 nM *X. fastidiosa* + 100 aM NsT (Xf high + NsT low), and 1 nM

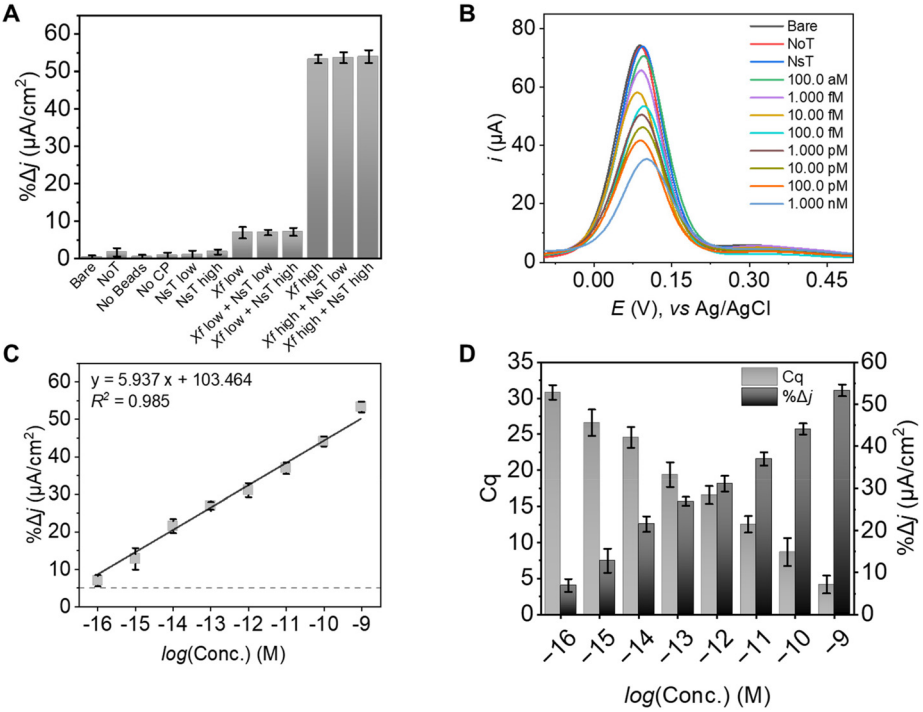

Fig. 3 Analytical performance of the assay using synthetic *Xylella fastidiosa* stDNA. (A) Percentage decrease in average current density for the bare electrode, no-target (NoT) control, no magnetic beads, no capture probe (CP), non-specific target (*X. albilineans*) at 100 aM (NsT-low) and 1 nM (NsT-high), and mixtures of low (100 aM) and high (1 nM) *X. fastidiosa* ssDNA with NsT-low and NsT-high synthetic DNA. (B) Representative DPV responses obtained for synthetic *X. fastidiosa* DNA over the concentration range 100 aM–1.0 nM. (C) Corresponding calibration curve showing the concentration-dependent increase in percentage current density decreases with increasing target DNA concentration. The dotted line indicates the LoD. (D) Correlation between the percentage decrease in average current density from DPV measurements and the corresponding C_q values obtained for the same synthetic *X. fastidiosa* DNA using standard PCR. Error bars represent the SD from three independent DPV and PCR measurements.

X. fastidiosa + 1 nM NsT (Xf high + NsT high). When *X. fastidiosa* stDNA was present at 100 aM, the mixtures produced current density changes comparable to those obtained with 100 aM *X. fastidiosa* alone, regardless of the NsT concentration. In contrast, mixtures containing 1 nM *X. fastidiosa* stDNA showed more than a 50% decrease in current density, similar to the response observed with 1 nM target alone and independent of the amount of NsT present. In all cases, the signal was determined by the concentration of the target *X. fastidiosa* stDNA, confirming that the assay remains selective even in the presence of high levels of non-specific DNA.

3.4 Assay sensitivity

The sensitivity of the assay was evaluated by measuring defined concentrations of *X. fastidiosa* stDNA prepared in nuclease-free water over a range from 100 aM to 1 nM (Fig. 3B and C). As the target concentration increased, the magnitude of the DPV current change systematically increased. This trend reflects greater adsorption of stDNA onto the Au-SPE, which progressively restricts access of ferricyanide ions to the electrode surface, thereby reducing the faradaic current and producing larger changes in the DPV current density. A clear concentration-dependent response was observed across the entire tested concentration range. The calibration plot of the current density change *versus* the logarithm of stDNA concentration showed a linear relationship described by the regression equation $y = 5.937x + 103.464$, with a coefficient of determination of $r^2 = 0.985$ (Fig. 3C). These data demonstrate that the assay provides a stable and semi-quantitative DPV response over more than seven orders of magnitude in target concentration. The data shown in Fig. 3C also represent the average of three independent experiments conducted using freshly prepared reagents and three separate Au-SPEs. Error bars indicate the standard deviation (SD) obtained from independent DPV measurements. Across the concentration range from 1 nM to 10 fM, the relative SD remained below 5% ($n = 3$), confirming good reproducibility and intra-assay precision. Minor variations observed in these measurements can be attributed primarily to electrode-to-electrode variability, small temperature fluctuations, and differences in sample handling.

The limit of detection (LoD) was calculated using the standard approach based on the background signal. The signal corresponding to the mean background response plus three times the SD of the background was used to define the LoD.[49] In Fig. 3C, this threshold is indicated by the dashed line, representing three times the SD of the current density change at zero concentration of the target DNA. Using this method, the LoD was estimated to be 100 aM, corresponding to roughly

300 copies per microliter. This attomolar-level sensitivity highlights the effectiveness of rapid, potential-induced adsorption of stDNA onto an unmodified Au-SPE.

Compared with existing detection methods for *X. fastidiosa*, the present assay offers a favourable balance between sensitivity and analysis time (Table S2). Real-time PCR[17] can detect as few as approximately 10 copies per microliter but typically requires around two hours from sample to result and involves thermal cycling and laboratory infrastructure. LAMP[17] and conventional PCR[17] also require longer assay times and multiple processing steps, with reported detection limits comparable to or higher than those achieved here. Several previously reported electrochemical and electronic biosensors show lower sensitivity than the present method. A copper(II)-based electrochemical biosensor[50] detected *X. fastidiosa* DNA only at submicromolar concentrations. Electrochemical impedance spectroscopy methods[51] reported detection limits on the order of 10^3 colony forming units (CFU) per milliliter, which is substantially less sensitive than the attomolar-level detection achieved here. An electrolyte-gated transistor platform[52] demonstrated detection of individual bacterial cells and provided a rapid response, but it requires more complex device fabrication and signal readout compared with the simple electrochemical setup used here. Importantly, the total analysis time of the present assay is approximately 30 minutes from purified target to DPV readout. This is significantly faster than PCR-based methods[17] and comparable to the fastest reported electronic sensing approaches,[50,51] while maintaining a detection limit of 100 aM.

3.5 qPCR validation

The electrochemical results shown in Fig. 3B and C were validated using qPCR, which is the gold standard method for *X. fastidiosa* detection. The qPCR assays were performed following an established protocol reported in ref. 17. This validation step was used to confirm that the DPV responses directly reflect the presence and concentration of the target DNA. As shown in SI Fig. S4, qPCR successfully amplified the *rimM gene* region from the *X. fastidiosa* 9a5c genome. A clear and systematic change in C_q values was observed across all tested target concentrations (SI Fig. S4A). Importantly, this trend closely matched the concentration-dependent changes observed in the DPV current densities for the same samples (Fig. 3D). Lower target concentrations produced higher C_q values, whereas higher target concentrations produced lower C_q values, in agreement with the corresponding DPV responses. No significant amplification was detected for the NsT and NoT controls. This absence of amplification is consistent with the negligible DPV signal changes observed for the same controls, confirming that both methods selectively detect the *X. fastidiosa* target DNA. Taken together, these validation results demonstrate that the developed method provides reliable detection of *X. fastidiosa* DNA and offers a rapid and simple alternative to qPCR without requiring enzymatic amplification or complex instrumentation.

3.6 Xylem sap extraction using a 3D printed device

The 3D printed sap extraction device (9 cm × 4 cm × 2.2 cm; Fig. 1A) enabled rapid and reproducible extraction of xylem sap from soft grapevine stems using simple mechanical compression. The device consistently produced measurable volumes of sap within a short time frame, demonstrating that controlled mechanical squeezing is sufficient to access xylem fluid without the need for external pressure sources, vacuum systems, or chemical treatments. Sap volumes on the order of tens of microliters were readily obtained from short stem segments, which is sufficient for most molecular and analytical assays.

A key advantage of this device is its portability and operational simplicity (for the operational procedure, see SI Fig. S1 and S2). Sap collection can be performed directly in the field or laboratory, with the extracted sap collected into standard PCR tubes. This format minimizes sample handling, reduces contamination risk, and allows immediate compatibility with downstream analytical methods. The short extraction time (~5 min) enables rapid sampling of multiple plants, which is important for surveillance studies and large-scale screening applications. Additionally, the device is fabricated by 3D printing using a common polymer material, which enables low-cost production, rapid prototyping, and easy modification of the design to accommodate different stem sizes or plant species. Because the extraction relies on mechanical compression rather than plant-specific anatomical features, the device can be readily adapted as a general tool for xylem sap collection from a wide range of soft-stemmed plants. This versatility makes it suitable for use across plant pathology, agriculture, and environmental monitoring studies.

Compared with previously reported approaches,[21,23] the 3D printed device offers several practical and analytical advantages. The silk fibroin microneedle platform reported by Cao *et al.*[21] enables direct interfacing with plant vasculature and continuous monitoring of sap composition. While powerful, this approach requires complex fabrication, careful insertion into plant tissue, and control over flow stability. Long-term field deployment may be affected by clogging, mechanical failure, variable sap pressure, and tissue heterogeneity. In addition, the limited internal volume of microneedles restricts the amount of sap available for downstream analysis, which can be a limitation for assays requiring larger sample volumes. The negative-pressure syringe-based method[23] reported for tomato stems provides a low-cost alternative but relies on manual assembly of syringes, tubing, and airtight seals. This setup increases handling time and introduces variability, particularly under field conditions where maintaining consistent sealing and alignment can be challenging. These factors reduce throughput and reproducibility when large numbers of samples are processed. In contrast, the 3D printed device described here operates as a single, self-contained unit and requires no manual pressure control, sealing steps, or auxiliary components. This simplicity improves reproducibility and makes the method well suited for high-throughput and on-site

sampling. The ability to collect sap directly into PCR tubes further streamlines integration with downstream analytical workflows.

3.7 Detection of *X. fastidiosa* in spiked xylem sap and qPCR validation

The applicability of the method to complex biological matrices was evaluated using xylem sap samples. Grapevine stems were collected from vineyards in Orange, NSW, Australia (Fig. 4A), transported to the laboratory, cleaned with 70% ethanol, and cut into approximately 3 cm segments for sap extraction. Xylem sap was obtained using the procedure described in Section 2.3 (SI Fig. 1 and 2). In the first set of experiments, all control measurements previously performed with spiked buffer samples (Fig. 3A) were repeated using spiked xylem sap. The changes in DPV current density observed for the NoT, no beads, no CP, and low and high concentrations of NsT control experiments were comparable to those obtained with the bare electrode. This behaviour is consistent with that observed in buffer for the corresponding control experiments (Fig. 3A). These results confirm the high specificity of the detection system in the presence of a complex sap matrix (Fig. 4D). Minor variations in current density changes were observed for samples containing high and low concentrations of NsT, as well as for mixtures containing different combinations of *X. fastidiosa* stDNA and NsT targets (see the last two bars in Fig. 4D). These variations were small, within the %RSD limits, and can be attributed to normal electrode-to-electrode variability, differences in sample handling, manual sap processing, and matrix effects associated with the presence of xylem sap.

In the second set of experiments, defined concentrations of *X. fastidiosa* stDNA were spiked into tenfold-diluted xylem sap to minimise the inhibitory effects of plant-derived compounds (*e.g.*, polyphenols and polysaccharides) while preserving a biologically relevant matrix, thereby enabling reliable evaluation of detection performance. Following magnetic isolation and purification, DPV measurements were carried out after the potential-induced adsorption step (Fig. 4E). A clear concentration-dependent decrease in current density was observed across the entire tested range, with the largest signal suppression occurring at the highest target concentration of 1 nM. The calibration plot of current density change *versus* the logarithm of stDNA concentration exhibited a linear relationship described by the regression equation $y = 6.620x + 113.459$, with a coefficient of determination of 0.986 (Fig. 4F). This linearity was maintained over more than seven orders of magnitude in target concentration. Across the concentration range from 1 nM to 10 fM (Fig. 4F), the relative standard deviation remained below 5% ($n = 3$), demonstrating good reproducibility and intra-assay precision. The LoD was estimated to be 100 aM, which is identical to that obtained in buffer, indicating that the sensitivity of the method is not compromised in a complex biological matrix.

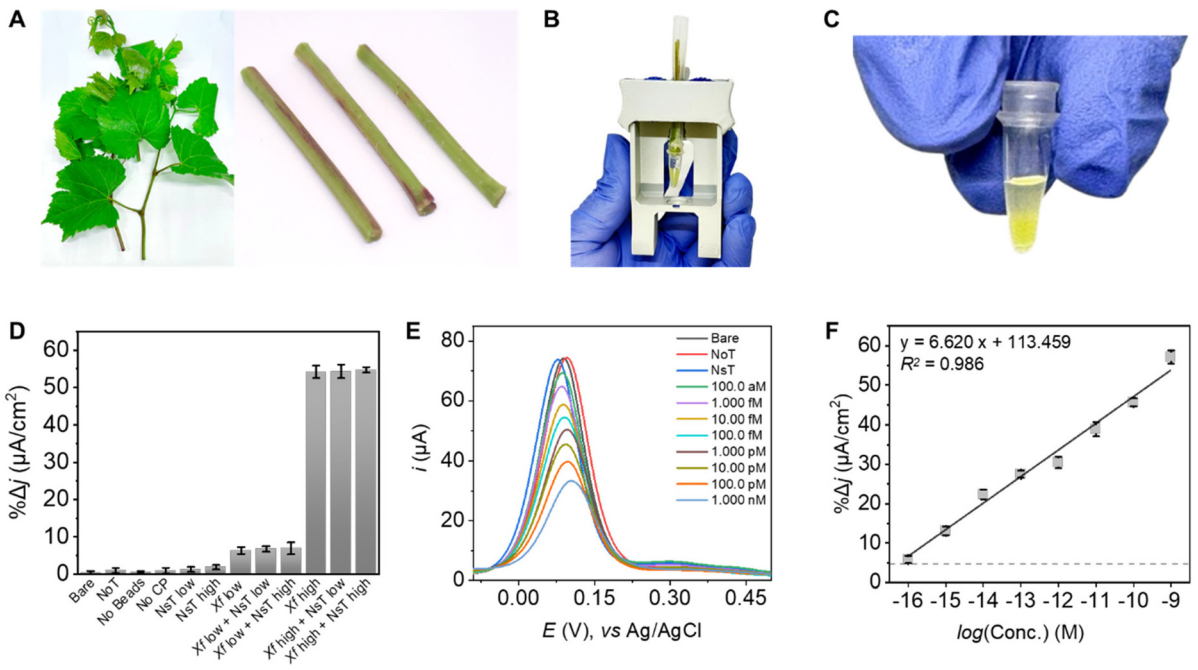

Fig. 4 Analytical performance of the assay using synthetic *Xylella fastidiosa* stDNA spiked into grapevine xylem sap. (A) Grapevine collection and prepared clean stems for sap extraction. (B) Handheld 3D-printed device used to extract xylem sap. (C) Collected sap in the collection tube. (D) Percentage decrease in average current density for the bare electrode, NoT, no magnetic beads, CP, non-specific target (*X. albilineans*) at 100 aM (NsT-low) and 1 nM (NsT-high), and mixtures of low (100 aM) and high (1 nM) *X. fastidiosa* ssDNA with NsT-low and NsT-high, all spiked in xylem sap. (E) Representative DPV responses for synthetic *X. fastidiosa* DNA (100 aM–1.0 nM) spiked in sap. (F) Corresponding calibration curve showing concentration-dependent suppression of current density; the dotted line indicates the LoD. Error bars represent the SD from three independent DPV measurements using separately prepared electrodes.

To further validate these results, qPCR analysis was performed using the same sap samples, following the approach applied to buffer-spiked samples (Fig. 3D). As shown in Fig. S4, qPCR successfully amplified the *rimM gene* region from the *X. fastidiosa* 9a5c genome, with a clear and systematic change in C_q values across all tested target concentrations. No significant amplification was observed for the non-specific target or no-template controls. The qPCR results closely matched the concentration-dependent trends observed in the DPV measurements and were fully consistent with the buffer-based validation data. The strong agreement between qPCR and DPV results confirms that the measured DPV signals originate from the target DNA rather than non-specific adsorption or matrix-induced background effects. Collectively, these findings demonstrate that the developed method enables reliable, sensitive, and specific detection of *X. fastidiosa* DNA directly in xylem sap samples.

4 Conclusion

This study introduces potential-induced DNA adsorption as a concept for agricultural diagnostics and demonstrates its application for detecting *X. fastidiosa*, a major plant health threat. By exploiting electrically driven interactions between nucleic acids and a gold electrode, the target DNA was captured and detected directly without enzymatic amplification. The resulting electrochemical readout was sensitive and selective, achieving a detection limit of 100 aM with negligible response to non-specific targets in spiked xylem sap. These findings confirm analytical performance in a complex biological matrix and support the feasibility of direct sap analysis. As this work represents a proof of concept, further validation across different plant species, infection stages, and field-collected samples is required to establish robustness under controlled laboratory conditions. The integrated workflow, combining portable xylem sap extraction with rapid electrochemical measurement, provides a practical foundation for subsequent translation beyond conventional laboratory settings.

The use of low-cost fabrication and minimal instrumentation supports scalability in agricultural environments. Importantly, the underlying detection principle is not target-specific. With appropriate probe design, the platform could be adapted to monitor a broad range of plant pathogens of biosecurity and agronomic concern. With further field-based validation and optimization, this approach has the potential to support earlier intervention, strengthen plant health surveillance, and enable more responsive disease management strategies across diverse cropping systems.

Author contributions

F. H.: conceptualization, data curation, formal analysis, investigation, methodology, validation, and writing – original draft. K. S.: formal analysis, methodology, validation, and writing – review & editing. F. Z. F.: data curation, formal analysis, investigation, methodology, supervision, validation, and writing – review & editing. M. C.: writing – review & editing. M. A. S.: formal analysis, validation, and writing – review & editing. M. T. T.: formal analysis, validation, and writing – review & editing. O. H. B. M.: formal analysis, validation, and writing – review & editing. S. A.: writing – review & editing. K. M. K.: writing – review & editing. T. H.: writing – review & editing. G. M. G: resources, supervision, validation, writing – original draft, and writing – review & editing. M. J. A. S.: conceptualization, funding acquisition, project administration, resources, supervision, writing – original draft, and writing – review & editing.

Conflicts of interest

The authors declare no competing financial interest.

Data availability

The data supporting this article have been included as part of the supplementary information (SI). Supplementary information: Fig. S1–S4 and Table S1. See DOI: https://doi.org/10.1039/d6an00096g.

Acknowledgements

F. H. acknowledges the support of a PhD scholarship from Charles Sturt University. M. J. A. S., K. M. K. and T. H. acknowledge funding from the Australian Government through the ARC Discovery Project (DP250101156).

References

1 Food and Agriculture Organization of the United Nations (FAO), *The hidden health crisis: How plant diseases threaten global food security*, FAO, Rome, 2025, https://www.fao.org/one-health/highlights/how-plant-diseases-threaten-global-food-security.
2 D. R. Paini, A. W. Sheppard, D. C. Cook, P. J. De Barro, S. P. Worner and M. B. Thomas, *Proc. Natl. Acad. Sci. U. S. A.*, 2016, **113**, 7575–7579.
3 M. S. Alqahtani, A. K. Elshahawi and S. M. Khalaf, *Sci. Rep.*, 2025, **15**, 32460.
4 A. Purcell, *J. Plant Pathol.*, 1997, **79**, 99–105.
5 European Food Safety Authority (EFSA), A. Delbianco, D. Gibin, L. Pasinato, D. Boscia and M. Morelli, *EFSA J.*, 2022, **20**, e07356.
6 S. Chatterjee, R. P. P. Almeida and S. Lindow, *Annu. Rev. Phytopathol.*, 2008, **46**, 243–271.

7 International Plant Protection Convention (IPPC), *DP 25: Xylella fastidiosa*, FAO, Rome, 2025, https://www.ippc.int/en/publications/86498/.
8 K. P. Tumber, J. M. Alston and K. B. Fuller, *Calif. Agric.*, 2014, **68**, 20–24.
9 G. P. Martelli, D. Boscia, F. Porcelli and M. Saponari, *Eur. J. Plant Pathol.*, 2016, **144**, 235–243.
10 M. Saponari, D. Boscia, F. Nigro and G. P. Martelli, *J. Plant Pathol.*, 2013, **95**, 668.
11 Australian Government, Department of Agriculture, Fisheries and Forestry, *International Symposium on Xylella fastidiosa: Biosecurity and Trade*, Canberra, 2024.
12 A. Hafi, L. R. Ahmed, T. Arthur, D. Addai, P. Tennant and J. Gomboso, in *Economic impacts of Xylella fastidiosa on the Australian wine grape and wine-making industries*, Australian Government, Department of Agriculture, Fisheries and Forestry, Canberra, 2023.
13 D. L. Hopkins and A. H. Purcell, *Plant Dis.*, 2002, **86**, 1056–1066.
14 R. P. Almeida, *Science*, 2016, **353**, 346–348.
15 European Food Safety Authority (EFSA), *EFSA J.*, 2015, **13**, 3991.
16 G. V. Minsavage, C. M. Thompson, D. L. Hopkins, R. M. Leite and R. E. Stall, *Phytopathology*, 1994, **84**, 456–461.
17 S. J. Harper, L. I. Ward and G. R. G. Clover, *Phytopathology*, 2010, **100**, 1282–1288.
18 EPPO, *EPPO Bull.*, 2010, **40**, 369–372.
19 P. J. Zarco-Tejada, C. Camino, P. S. A. Beck, R. Calderón, A. Hornero, R. Hernández-Clemente, *et al.*, *Nat. Plants*, 2018, **4**, 432–439.
20 P. A. Zaini, L. De La Fuente, H. C. Hoch and T. J. Burr, *FEMS Microbiol. Lett.*, 2009, **295**, 129–134.
21 Y. Cao, D. Kim, S. S. Koh, Z. Li, F. Rigoldi, J. E. Fortmueller, *et al.*, *Nat. Nanotechnol.*, 2025, **20**, 1–10.
22 M. Kan, K. Yamazaki, T. Fujiwara and T. Kamiya, *BioTechniques*, 2019, **67**, 242–245.
23 B. Longchar, T. Phukan, S. Yadav and M. Senthil-Kumar, *Appl. Plant Sci.*, 2020, **8**, e11335.
24 K. M. Koo, F. Z. Farhana, A. G. Ross and M. J. A. Shiddiky, *Anal. Chem.*, 2025, **97**, 2579–2587.
25 K. M. Koo, A. A. I. Sina, L. G. Carrascosa, M. J. A. Shiddiky and M. Trau, *Anal. Methods*, 2015, **7**, 7042–7054.
26 A. A. I. Sina, L. G. Carrascosa, R. Palanisamy, S. Rauf, M. J. A. Shiddiky and M. Trau, *Anal. Chem.*, 2014, **86**, 10179–10185.
27 K. M. Koo, L. G. Carrascosa, M. J. A. Shiddiky and M. Trau, *Anal. Chem.*, 2016, **88**, 2000–2005.
28 K. M. Koo, A. A. I. Sina, L. G. Carrascosa, M. J. A. Shiddiky and M. Trau, *Analyst*, 2014, **139**, 6178–6184.
29 P. Sambasivam, M. Bilkiss, N. Soda, I. Bar, M. J. A. Shiddiky and R. Ford, *ACS Agric. Sci. Technol.*, 2024, **4**, 1184–1193.
30 M. Chakraborty, S. A. Bhuiyan, S. Strachan, M. J. A. Shiddiky, N.-T. Nguyen, N. Soda and R. Ford, *Adv. Sens. Res.*, 2025, **4**, 2400103.
31 M. Chakraborty, S. A. Bhuiyan, S. Strachan, M. J. Shiddiky, N.-T. Nguyen, N. Soda and R. Ford, *Biosensors*, 2025, **15**, 518.
32 K. Dyussembayev, P. Sambasivam, I. Bar, J. C. Brownlie, M. J. A. Shiddiky and R. Ford, *Front. Chem.*, 2021, **9**, 636245.
33 I. Pieretti, M. Royer, V. Barbe, S. Carrere, R. Koebnik, S. Cociancich, A. Couloux, A. Darrasse, *et al.*, *BMC Genomics*, 2009, **10**, 616.
34 Y. Chen, W. Ye, Y. Zhang and Y. Xu, *Nucleic Acids Res.*, 2015, **43**, 7762–7768.
35 J. Zhang, S. Song, L. Wang, D. Pan and C. Fan, *Nat. Protoc.*, 2007, **2**, 2888–2895.
36 M. J. A. Shiddiky, A. A. Torriero, C. Zhao, I. Burgar, G. Kennedy and A. M. Bond, *J. Am. Chem. Soc.*, 2009, **131**, 7976–7989.
37 M. H. Haque, V. Gopalan, S. Yadav, M. N. Islam, E. Eftekhari, Q. Li, L. G. Carrascosa, N.-T. Nguyen, A. K. Lam and M. J. A. Shiddiky, *Biosens. Bioelectron.*, 2017, **87**, 615–621.
38 W. Wang, X. Ding, M. He, J. Wang and X. Lou, *Anal. Chem.*, 2014, **86**, 10186–10192.
39 F. Ricci, N. Zari, F. Caprio, S. Recine, A. Amine, D. Moscone, G. Palleschi and K. W. Plaxco, *Bioelectrochemistry*, 2009, **76**, 208–213.
40 P. K. Das, O. Adil and M. H. Shamsi, *ACS Appl. Nano Mater.*, 2025, **8**, 6797–6817.
41 Y. A. Alsunni and C. B. Musgrave, *Appl. Surf. Sci.*, 2023, **610**, 155147.
42 P. Peljo, J. A. Manzanares and H. H. Girault, *Langmuir*, 2016, **32**, 5765–5775.
43 B. P. Fingerhut, *Chem. Commun.*, 2021, **57**, 12880.
44 R. Garcia, *ACS Nano*, 2023, **17**, 51–69.
45 J. J. Cartus, A. Jeindl, A. Werkovits, L. Hörmann and O. T. Hofmann, *Nanoscale Adv.*, 2023, **5**, 2288–2298.
46 Z. Long, J. Meng, L. R. Weddle, P. E. Videla, J. P. Menzel, D. G. A. Cabral, J. Liu, T. Qiu, J. M. Palasz, D. Bhattacharyya, C. P. Kubiak, V. S. Batista and T. Lian, *Chem. Rev.*, 2025, **125**, 1604–1628.
47 X. Zhang, M. R. Servos and J. Liu, *Langmuir*, 2012, **28**, 3896–3902.
48 J. Liu, *Phys. Chem. Chem. Phys.*, 2012, **14**, 10485–10496.
49 D. M. Rissin, C. W. Kan, T. G. Campbell, S. C. Howes, D. R. Fournier, L. Song, T. Piech, P. P. Patel, L. Chang, A. J. Rivnak and E. P. Ferrell, *Nat. Biotechnol.*, 2010, **28**, 595–599.
50 W. Machini and A. M. Oliveira-Brett, *Electrochem. Commun.*, 2021, **125**, 106975.
51 M. S. Chiriacò, A. Luvisi, E. Primiceri, E. Sabella, L. De Bellis and G. Maruccio, *Sci. Rep.*, 2018, **8**, 7376.
52 L. Sarcina, E. Macchia, G. Loconsole, G. D'Attoma, P. Bollella, M. Catacchio, *et al.*, *Adv. Sci.*, 2022, **9**, 2203900.